PHOTONICS Research

Geometric-phase-induced arbitrary polarization and orbital angular momentum generation in helically twisted birefringent photonic crystal fiber

TAKESHI FUJISAWA* AND KUNIMASA SAITOH [iD]

Graduate School of Information Science and Technology, Hokkaido University, Japan
Corresponding author: fujisawa@ist.hokudai.ac.jp

The evolutions of polarization and orbital angular momentum (OAM) states of light in helically twisted birefringent photonic crystal fibers (TB-PCFs) are analyzed. It is shown that a circular polarization (CP) component (S_3 of a Stokes parameter) is periodically excited when usual linearly polarized (LP) modes of PCF are launched. The excitation originates from a geometric phase in TB-PCFs. The S_3 excitation is larger for larger linear birefringence for a fixed twisting rate. If the linear birefringence is large enough, a CP filtering behavior can be seen in addition to the S_3 excitation. From the analytical consideration of the sign of the geometric phase, the TB-PCF with periodical inversion of twisting is proposed to generate arbitrary polarization state on the Poincaré sphere. Next, an OAM state generation in multimode TB-PCFs is shown for higher-order LP mode input. By observing a far-field interference pattern from TB-PCF mixed with LP_{01} mode, a vortex associated with the OAM state can be seen. Similar to the single-mode case, by using periodical twisting inversion, efficient OAM generation is possible. These results indicate that by simply launching fiber's LP mode into TB-PCF, arbitrary polarization and OAM states can be generated, leading to a novel mechanism for the manipulation of the spatial state of light. © 2020 Chinese Laser Press

https://doi.org/10.1364/PRJ.393255

1. INTRODUCTION

A chiral fiber grating (CFG) is an attractive candidate for controlling various spatial states of light, such as polarization, guided mode, and optical angular momentum (OAM). From the first report of a circular polarized light filtering behavior in CFG [1] with birefringent core, many experimental works have been reported, such as polarization-dependent filtering in single- and double-helix fiber [2]. To explain complex polarization behavior in the CFGs, theoretical studies have also been conducted [3,4]. In Ref. [4], the guided modes in elliptical core twisted fibers (double-helix) were intensively studied, and the coupling between core and cladding modes affects the transmission characteristics and the selection rule of the coupling was proposed. In these studies, only the guided mode of the twisted fiber was investigated, and the longitudinal evolution of the spatial state of light has hardly been discussed.

Recently, helically twisted photonic crystal fibers (PCFs) were proposed and fabricated [5] that have periodic dips in the transmission spectra originating from the coupling between core and cladding modes with OAM. After this report, many unique features of twisted PCF were discovered, such as an

optical activity and a circular dichroism [6–8], higher-order OAM mode generation [9] at a wavelength near the dip, and a circular-polarized mode filtering in off-axis core twisted PCFs [10]. In PCFs, it is easy to incorporate the linear birefringence by changing the size of a part of air holes. The magnitude of the linear birefringence can also be easily tuned with the size of air holes. Therefore, twisted birefringent PCFs (TB-PCFs) can be viewed as a new kind of CFG and a good platform for controlling the spatial state of light.

In Ref. [11], a preliminary work on TB-PCF was presented. Formulating the light propagation in single-mode TB-PCF with a periodically inverted twisting based on a transfer-matrix approach, the theoretical analysis of the polarization state, group velocity dispersion, and adiabatic connection to usual fiber were demonstrated. However, important physical phenomena in twisted fibers, such as circular dichroism, discovered by full-vector modeling methods [6–8], were not demonstrated. Also, a uniform TB-PCF was not treated. Furthermore, the formulation was done with the two modes (x and y modes), and OAM generation with the topological charge >0, which is an important topic for twisted fibers, was not treated.

In this paper, the polarization (including OAM) state of TB-PCFs is thoroughly investigated with the full-vector analysis method. It is shown that a circular polarization (CP) component (S_3 of the Stokes parameters) is periodically excited [12] in uniform TB-PCFs when usual linearly polarized (LP) modes of a PCF are launched. The periodic excitation is interpreted as an effect of a geometric phase [13] in TB-PCFs. The S_3 excitation is larger for larger linear birefringence for a fixed twisting rate. If the linear birefringence is large enough, a CP filtering behavior can be seen in addition to the S_3 excitation. From the analytical consideration of the sign of the geometric phase, the method for efficiently accumulating the phase difference between two CPs is discovered. Based on this idea, TB-PCFs with periodical inversion of the twisting are analyzed to generate an arbitrary polarization state on the Poincaré sphere. Next, the polarization state of the multimode TB-PCFs is investigated for the first time. An OAM state generation in multimode TB-PCFs is shown for higher-order LP mode input. By observing a far-field interference pattern (FFIP) from TB-PCF mixed with LP$_{01}$ mode, a vortex associated with the OAM state can be seen. Similar to the single-mode case, with the periodical twisting inversion, efficient OAM generation is possible. These phenomena are analyzed by the recently developed rigorous full-vector beam propagation method (BPM) specially formulated for helicoidal waveguides [14–16], which can explain the experimental transmission spectra and polarization states of helically twisted PCFs, both qualitatively and quantitatively. By using the helical BPM, it is possible to track the longitudinal evolution of the polarization state in the fiber with an arbitrary input condition by considering important physical phenomena, such as CP filtering, which is difficult for conventional analysis methods based on guided mode analysis. The results shown in this paper make the understanding of optical physics in twisted waveguides deeper and are useful for fiber-based polarization and OAM controlling devices [17–20], since it adds new degrees of freedom to control the spatial state of light.

2. BPM FOR HELICOIDAL WAVEGUIDES

In the theoretical analysis of helically twisted PCFs, a guided mode analysis based on the finite-element method (FEM) formulated for helical systems [21–23] has been used. In this FEM, the concept of transformation optics [24] is used for the formulation, namely, the helically twisted structure is replaced with a straight waveguide with equivalent permittivity, ε, and permeability, μ, tensors. For the twisted waveguides, left CP and right CP (LCP and RCP) modes are obtained from this guided mode analysis and much information can be extracted. However, it is difficult to treat longitudinal evolution of the spatial state of light in a waveguide with arbitrary input conditions. For example, in most experiments, the input light seems not to be in the CP mode, but in the LP mode. Therefore, a BPM analysis is more suitable for investigating the longitudinal behavior of the spatial state of light in the twisted waveguides. Here, we briefly summarize the BPM for helicoidal waveguides.

We consider a helically TB-PCF, shown in Fig. 1. The origin is at the center of the fiber. The cladding is composed of
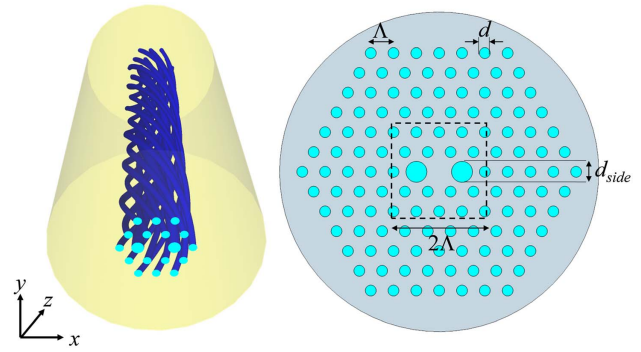

Fig. 1. Schematic of (left) three-dimensional structure and (right) cross section of TB-PCF. The number of rings in the three-dimensional sketch is reduced for clarity. The simulation is carried out for the cross section shown in the right panel. The dashed lines are a square with the side length of 2Λ. The inside area is used to calculate the Poynting vector in the core.

hexagonally arranged air holes with diameter d and pitch Λ. There are six rings of air holes, and there is no air hole at the center of the array that forms the core. The diameters of two side holes adjacent to the core are d_{side}. If $d = d_{side}$, there is no linear birefringence. The computational window is a circle, and the outer region is a cylindrical perfectly matched layer (CPML) region with a thickness d_{PML}. The fiber is helically twisted along the z direction with a twisting rate of α [rad/m]. The propagation direction is z, and xy is the transverse plane. The transformation between helical and modeling coordinates is given by

$$x' = x \cos(\alpha z) + y \sin(\alpha z), \tag{1a}$$

$$y' = -x \sin(\alpha z) + y \cos(\alpha z), \tag{1b}$$

$$z' = z. \tag{1c}$$

Here, the notations x, y, and z denote the modeling coordinates, in which the numerical discretization is made, and x', y', z' are the original coordinates. Due to the equivalence under the coordinate transformation of Maxwell's equations, the following wave equation is satisfied for both coordinates:

$$\nabla \times (\boldsymbol{\mu}_r^{-1} \nabla \times \boldsymbol{E}) - k_0^2 \boldsymbol{\varepsilon}_r \boldsymbol{E} = \boldsymbol{0}, \tag{2}$$

where $\boldsymbol{E}$ is the electric field vector, $\boldsymbol{\varepsilon}_r$ and $\boldsymbol{\mu}_r$ are the relative permittivity and permeability tensors, and k_0 is the free-space wavenumber. In the modeling coordinate, $\boldsymbol{\varepsilon}_r$ and $\boldsymbol{\mu}_r$ are modified due to the coordinate transformation, and are given by

$$\boldsymbol{\varepsilon}_r = n^2(x, y, z) \boldsymbol{T}_{metric}^{-1}, \tag{3}$$

$$\boldsymbol{\mu}_r = \boldsymbol{T}_{metric}^{-1}. \tag{4}$$

Here, we assume an ordinary optical isotropic medium with a refractive index of n and a relative permeability of 1 in the original coordinate. $\boldsymbol{T}_{metric}$ is a metric tensor and is given by

T_{metric}

$$= \frac{J^T J}{\det J}$$

$$= \begin{bmatrix} s\cos^2\phi + s^{-1}\sin^2\phi & (s-s^{-1})\sin\phi\cos\phi & \alpha r s^{-1}\sin\phi \\ (s-s^{-1})\sin\phi\cos\phi & s\sin^2\phi + s^{-1}\cos^2\phi & -\alpha r s^{-1}\cos\phi \\ \alpha r s^{-1}\sin\phi & -\alpha r s^{-1}\cos\phi & s^{-1}(1+\alpha^2 r^2) \end{bmatrix},$$

$$(5)$$

where J is the Jacobian matrix between the helical and Cartesian systems. By using these tensors given by Eqs. (3) and (4), we can treat the twisted PCF as a simple straight waveguide. We consider a propagating field with reference index n_0 in the positive z direction as

$$E(x,y,z) = e(x,y,z)\exp(-jk_0 n_0 z). \quad (6)$$

By substituting Eq. (6) into Eq. (2) and discretizing the waveguide cross section with full-vector FEM, we can obtain marching equations used for BPM. Detailed formulation can be found in Refs. [14,15] together with qualitative and quantitative comparisons with experimental transmission spectra.

3. TRANSMISSION CHARACTERISTICS OF TB-PCF

A. Basic Characteristics

We consider TB-PCF, shown in Fig. 1, with $d = 1.1$ μm and $\Lambda = 2.9$ μm. We added a CPML region with the thickness of $d_{\text{PML}} = 2$ μm outside the analysis region (a circle with the radius of 20 μm). The air hole at the center of the fiber is missing to form the core, and diameters of the two holes adjacent to the core in the x direction are changed to d_{side}. The refractive index of silica is calculated by the Sellmeier formula described in

Ref. [25]. The top left panel of Fig. 2 shows the effective refractive index (n_{eff}) of PCF without twisting ($\alpha = 0$) as a function of d_{side}. In this paper, the wavelength of the light is $\lambda = 1.2$ μm. The n_{eff} of the y-polarized mode ($n_{\text{eff},y}$) is larger than that of the x-polarized mode ($n_{\text{eff},x}$) because the air hole in the x direction is large. In the same figure, the linear birefringence of the PCF as a function of d_{side} is shown. The linear birefringence is given by

$$B = n_{\text{eff},x} - n_{\text{eff},y}. \quad (7)$$

For larger values of d_{side}, the absolute value of B becomes larger, and it is larger than 2×10^{-4} for $d_{\text{side}} > 2$ μm. The top right panel of Fig. 2 shows a polarization beat length (L_{pol}) and polarization twisting rate (α_{pol}) as functions of d_{side}. L_{pol} and α_{pol} are given by

$$L_{\text{pol}} = \frac{\lambda}{|B|}, \quad (8)$$

$$\alpha_{\text{pol}} = \frac{2\pi}{L_{\text{pol}}}. \quad (9)$$

The effect of α_{pol} and the twisting rate of the fiber α will be discussed later.

The bottom panel of Fig. 2 shows n_{eff} of the fundamental modes of PCF as a function of α for different values of d_{side} calculated by helical FEM [21–23]. The circular birefringence [6] can be seen as a split of n_{eff} to upper and lower branches. One corresponds to RCP and the other corresponds to LCP. The linear birefringence affects the modes much more for lower values of α.

B. Polarization States in TB-PCF

Figure 3 shows the optical power in the core of TB-PCFs as a function of propagation distance for $d_{\text{side}} = 1.5$, 2, and
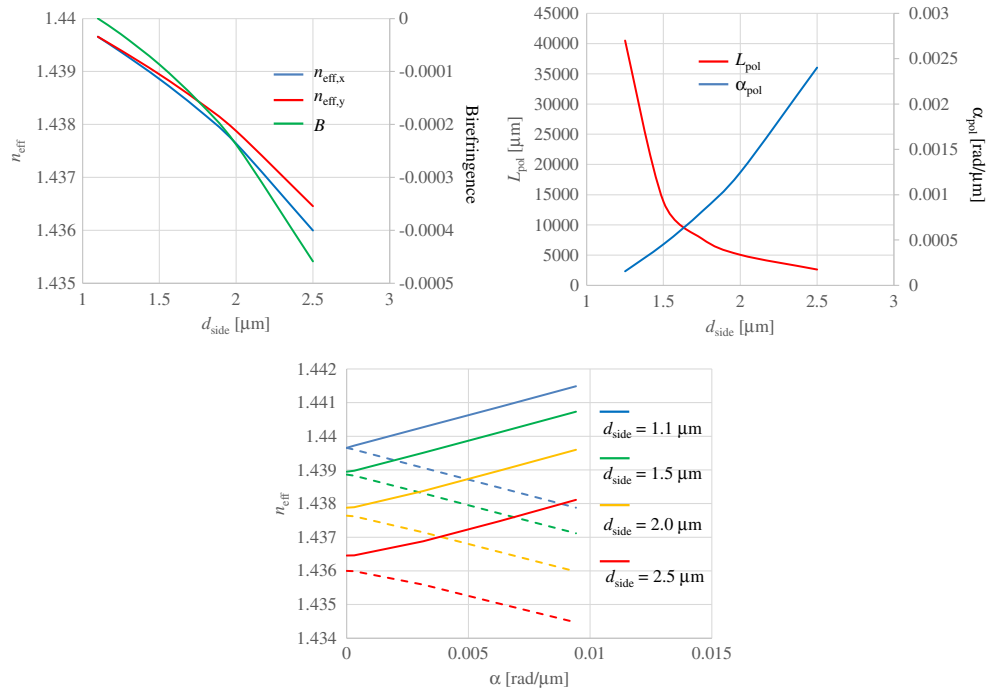

Fig. 2.   (Top left) n_{eff} and B and (top right) L_{pol} and α_{pol} as functions of d_{side}, and (bottom) n_{eff} as a function of the twisting rate.
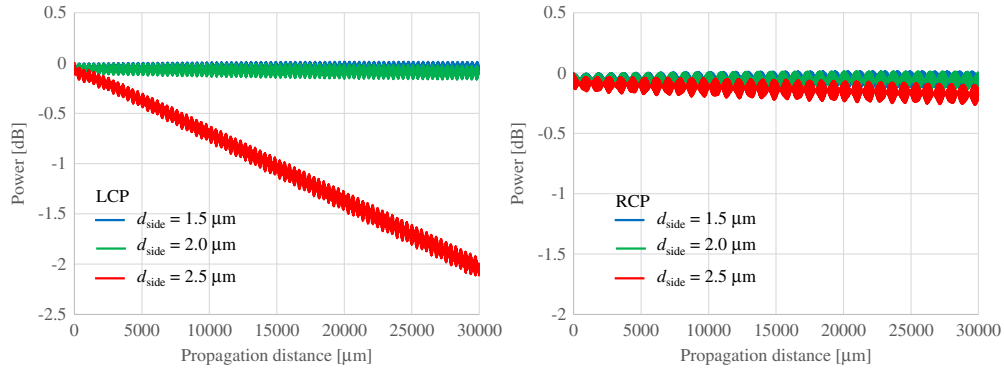
Fig. 3. Optical power in the core of TB-PCFs as a function of propagation distance for different values of d_{side}. Input modes are (left) LCP and (right) RCP modes. $\alpha = 0.006$ rad/μm.

2.5 μm. The step size in the BPM simulation is 10 μm. The twisting rate is $\alpha = 0.006$ rad/μm. Here, the positive value of α corresponds to counterclockwise rotation from the viewpoint of $+z$. The input light is LCP (Fig. 3, left) or RCP (Fig. 3, right) and obtained by summing orthogonal fundamental modes with a 90° phase difference, namely,

$$\boldsymbol{E}_{\pm} = \boldsymbol{E}_x \pm j\boldsymbol{E}_y, \tag{10}$$

where $\boldsymbol{E}_x$ and $\boldsymbol{E}_y$ correspond to the x- and y-polarized fundamental modes of non-twisted PCF calculated by full-vector FEM [26]. The plus sign is for RCP and the minus sign is for LCP. Here, the optical power in the core is defined as the Poynting vector surrounded by the dashed line in the right panel of Fig. 1 (square with the side length of 2Λ). For $d_{side} < 2.0$ μm (small linear birefringence), the loss difference between LCP and RCP is <0.1 dB after 30,000 μm propagation. For large linear birefringence with $d_{side} = 2.5$ μm, the loss of the LCP mode is larger than that of the RCP mode, and the difference is large (1.7 dB after 30 mm propagation, or 57 dB/m), showing the emergence of circular dichroism [7] due to the twisting. The left panel of Fig. 4 shows Stokes parameters S_1, S_2, and S_3 (normalized by S_0) calculated by BPM as a function of the propagation distance for TB-PCF with $d_{side} = 2.0$ μm and $\alpha = 0.006$ rad/μm. The x-polarized fundamental mode (E_x mode) of non-twisted PCF is launched (E_x input). Stokes parameters [27] are evaluated by

$$S_0 = \left(\int |E_x| dS \right)^2 + \left(\int |E_y| dS \right)^2, \tag{11a}$$

$$S_1 = \left(\int |E_x| dS \right)^2 - \left(\int |E_y| dS \right)^2, \tag{11b}$$

$$S_2 = 2 \int |E_x| dS \int |E_y| dS \cos(\phi_y - \phi_x), \tag{11c}$$

$$S_3 = 2 \int |E_x| dS \int |E_y| dS \sin(\phi_y - \phi_x), \tag{11d}$$

where $\phi_y - \phi_x$ is the phase difference between E_y and E_x at the center of the core. The integration is done over the cross section of the fiber. In this paper, S_1, S_2, and S_3 are normalized by S_0 at each propagation step. Note that these Stokes parameters can be used for the LP_{01} mode only, which has the maximum

field at the center of the core. From Fig. 4, there are two distinct features in the Stokes parameters. First, S_1 and S_2 are periodically exchanged. The period corresponds to the period of fiber twisting, and the phenomenon can be explained as follows. At the start, $S_1 = 1$ because E_x mode is input. After a 90° rotation, the polarization becomes y polarized ($S_1 = -1$) and after a 180° rotation, the polarization becomes x polarized again. This is so-called optical activity. Second, S_3 is periodically excited. After a 90° rotation, the absolute value of S_3 is at a maximum, and after 180° rotation, the value becomes 0 again. The right panel of Fig. 4 shows S_3 as a function of propagation distance for PCFs with $d_{side} = 1.1$, 1.5, and 2.0 μm as well as $\alpha = 0.006$ rad/μm. For $d_{side} = 1.1$ μm, there are no excitations of S_3, since there is no linear birefringence. For $d_{side} = 1.5$ and 2.0 μm, the periodic excitation of S_3 can be seen, and the magnitude of excitation is larger for large linear birefringence. Since it is difficult to explain this complex polarization evolution (the periodic excitation of S_3) with only the BPM results, we formulate a simple analytical beam propagation model based on a weak guiding approximation, which is summarized in the Appendix A. Key results are summarized as follows.

We consider a twisted birefringent waveguide shown in Fig. 16 in the Appendix A. The waveguide is twisted along the z direction, and an azimuthal rotation angle is $\theta = \alpha z$. We assume that the reference indices for x- and y-polarized modes are n_x and n_y when $\theta = 0$. From the analytical results of the propagation equation for x- and y-polarized modes, two basis transformations are performed, namely, xy to eo basis and eo to RCP-LCP basis. Finally, we obtain the propagation equation as

$$\Psi_{RL}(z + \Delta z) = \boldsymbol{U}_{RL}(\theta)\Psi_{RL}(z), \tag{12}$$

$$\boldsymbol{U}_{RL} = \boldsymbol{P}^{-1}\boldsymbol{U}_{eo}\boldsymbol{P} = e^{-jk_0 n_{ave}\Delta z} \begin{bmatrix} \cos\gamma & j\sin\gamma e^{-2j\theta} \\ j\sin\gamma e^{2j\theta} & \cos\gamma \end{bmatrix}, \tag{13}$$

where Ψ_R and Ψ_L are complex fields of RCP and LCP components. Other symbols are defined in the Appendix A. Here, an additional phase given by $e^{2j\theta}$ with the opposite sign in nondiagonal terms is called the "geometric phase." By using these equations, the evolution of input light (CP or LP modes) in the rotated frame can be calculated easily. If Δz is sufficiently small,
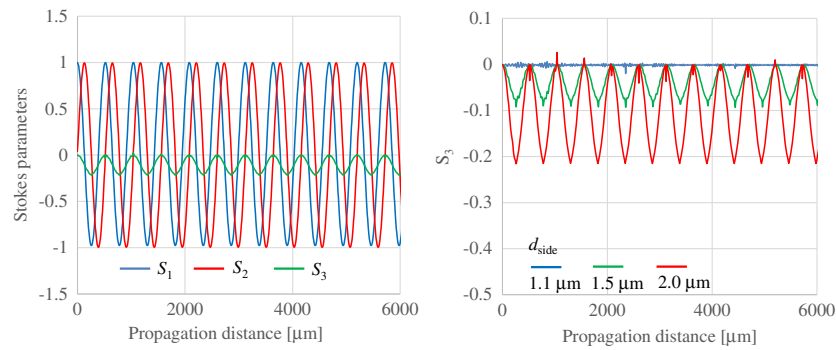
Fig. 4. (Left) Stokes parameters of TB-PCF for $d_{side} = 2.0$ μm and $\alpha = 0.006$ rad/μm and (right) S_3 of TB-PCF for different values of d_{side} calculated by BPM.
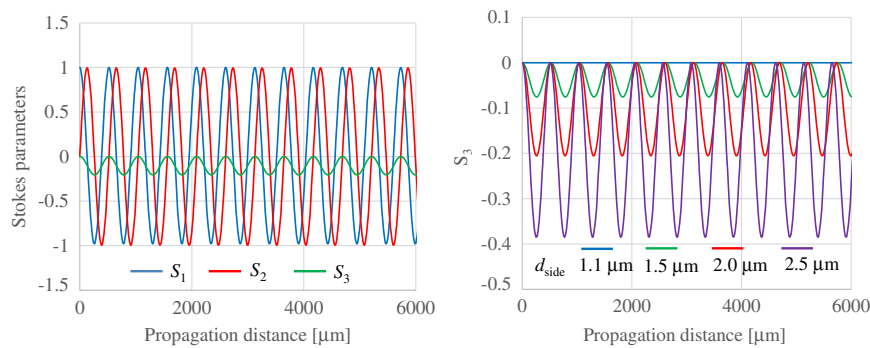

Fig. 5. (Left) Stokes parameters of TB-PCF for $d_{side} = 2.0$ μm and $\alpha = 0.006$ rad/μm and (right) S_3 of TB-PCF for different values of d_{side} calculated by the analytical method.

the beam propagation in the twisted waveguides can be treated by concatenating two segments, θ and $\theta + \Delta\theta$.

The left and right panels of Fig. 5 show the same data as in Fig. 4, but calculated by the analytical method (in the right panel of Fig. 5, the results for $d_{side} = 2.5$ μm are added). From the left panel of Fig. 5, it is shown that the optical activity (periodic exchange of S_1 and S_2) and the periodic excitation of S_3 can be reproduced. The way to understand the phenomena is the term of $e^{2j\theta}$ contained in Eq. (13). If the value of $\theta = 0$, S_3 excitation disappears, and therefore, the physical reason for the periodic excitation of S_3 can be attributed to the geometric phase [13], existing in twisted waveguides. From Fig. 5, the magnitudes of excitation of S_3 are consistent with BPM results and are larger for larger linear birefringence. However, the behavior is different from the analytical results for larger values of B. Figure 6 shows S_3 as a function of propagation distance for PCF with $d_{side} = 2.5$ μm with $\alpha = 0.006$ rad/μm calculated by the analytical method and BPM. The polarization behavior becomes more complex compared with the analytical results shown in Fig. 5. Negative S_3 (LCP) is first excited periodically as in the analytical results; however, around 5000 μm, the S_3 leans to the positive (RCP) side. The effect can be explained by the circular dichroism shown in Fig. 3. Since the loss of LCP is larger than that of RCP in TB-PCF with $d_{side} = 2.5$ μm, the LCP component contained in E_x mode is lost during propagation (the LP mode can be expressed

by the sum of LCP and RCP modes). Due to the loss difference, the S_3 gradually approaches the RCP side for long-distance propagation.

Figure 7 shows S_3 as a function of propagation distance for PCF with $d_{side} = 1.5$, 2.0, and 2.5 μm with $\alpha = 0.006$ rad/μm for E_y mode input. For low linear birefringence ($d_{side} = 1.5$ and 2.0 μm), completely opposite polarization is excited compared with the E_x mode input. For large linear birefringence ($d_{side} = 2.5$ μm), the polarization state rapidly approaches the RCP side because the LCP component is
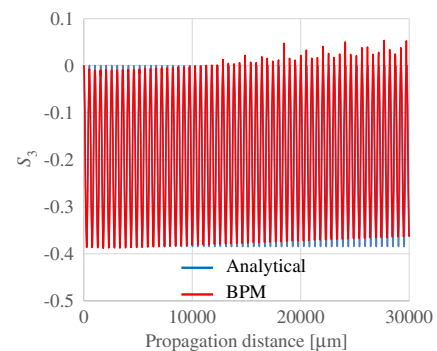

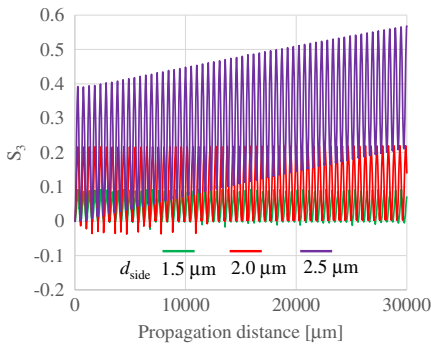**Fig. 6.** S_3 as a function of propagation distance for $d_{side} = 2.5$ μm with $\alpha = 0.006$ rad/μm.

Fig. 7. S_3 as a function of propagation distance for $\alpha = 0.006$ rad/μm and different values of d_{side}. E_y mode is launched.

not excited for E_y mode input and the LCP components contained in E_y mode are lost due to the circular dichroism during propagation.

Summarizing the results so far, the polarization behavior in the TB-PCFs is very complex, depending on the magnitude of the linear birefringence. For the PCF with small linear birefringence, there are two features in their polarization state, namely, optical activity and periodical excitation of S_3, originating from the geometric phase. For the PCF with large linear birefringence, in addition to the above features, the circular dichroism makes the polarization behavior more complex.

C. Effect of Twisting Rate

The left panel of Fig. 8 shows the optical power of TB-PCFs as a function of propagation distance for $d_{\mathrm{side}} = 2.5$ μm. The twisting rate is $\alpha = 0.0024$, 0.006, and 0.01 rad/μm. The input light is LCP or RCP mode. For a larger twisting rate, the circular dichroism is also larger, since, for a large twisting rate, many cladding modes are phase-matched to the core mode [28,29]. The right panel of Fig. 8 shows S_3 as a function of propagation distance for PCF with $d_{\mathrm{side}} = 2.5$ μm for E_x mode input. The magnitude of periodical excitation of S_3 is maximum for $\alpha = 0.0024$ rad/μm and is smaller for the larger twisting rate. This is because $\alpha_{\mathrm{pol}} \simeq \alpha = 0.0024$ rad/μm, as shown in Fig. 2. For $\alpha = 0.01$ rad/μm, the polarization state approaches the RCP side due to the large circular dichroism. From these results, the periodical excitation of S_3 becomes large when the twisting rate of the fiber is similar to that of the polarization twisting rate. For the large twisting rate, due to the phase matching to the cladding mode, the circular dichroism becomes large and CP filtering behavior can be seen.
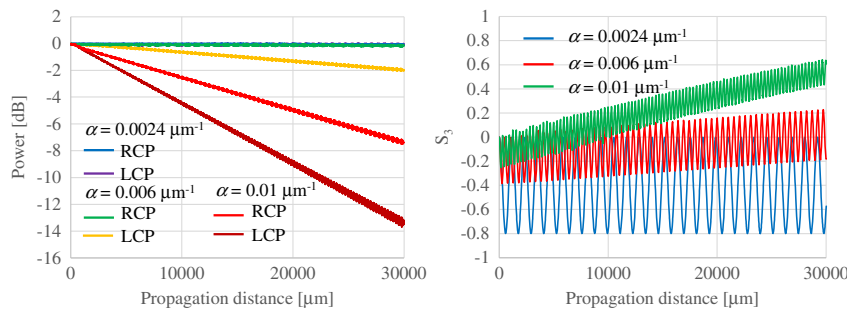
D. Wavelength Dependence

The left panel of Fig. 9 shows the transmission spectra of TB-PCFs as a function of propagation distance for different values of d_{side} and the twisting rate of $\alpha = 0.006$ rad/μm. The input light is in the E_x mode, and the fiber length is 30,000 μm. For $d_{\mathrm{side}} < 2.0$ μm, there are several decibel losses in the shown wavelength range. For $d_{\mathrm{side}} = 2.5$ μm, the loss increases due to the circular dichroism, especially for the long wavelength side. The center panel of Fig. 9 shows S_3 as a function of propagation distance for different wavelengths, and the right panel is the enlarged view. For the long wavelength side, the excitation of S_3 in one period is larger. This is because α_{pol} is close to α for the long wavelength side. For long-distance propagation, S_3 leans toward the RCP side due to the large loss of the LCP mode. The slope for the RCP mode is larger for the long wavelength due to the larger LCP loss.

E. Periodic Inversion of Twisting

From the results in Fig. 4, when the E_x mode is launched, the negative S_3 is excited, and the absolute value of the S_3 component is at a maximum at 90° rotation and then returned to zero at 180° rotation. Therefore, the accumulated phase shift between 0° and 90° is canceled out between 90° and 180° rotation. If the sign of the geometric phase can be inverted between 90° and 180° rotation, the accumulated phase shift is not canceled out and continuously accumulated, leading to a larger S_3 excitation. The sign inversion of the geometric phase can be achieved by changing the direction of twisting (the sign of α) periodically, as shown in the inset of Fig. 10, where $\Lambda_{\mathrm{twist}} = 2\pi/\alpha$. Although the fabrication of the structure is not easy, it is interesting to see what happens if the structure can be fabricated. According to Ref. [5], a permanent twist can be produced with proper processing. Therefore, multiple splicing of inverted sections may be one of the fabrication methods. Also, the length of each region cannot be $\Lambda_{\mathrm{twist}}/4$. Since the excitation of S_3 is periodic, the length should be $N\Lambda_{\mathrm{twist}} + \Lambda_{\mathrm{twist}}/4$ (N is an integer), and the length of each section can be lengthened.

The left panel of Fig. 10 shows Stokes parameters calculated by the analytical method for TB-PCF with $d_{\mathrm{side}} = 2.0$ μm and $\alpha = 0.0024$ rad/μm. The E_x mode is launched, and the sign of α is periodically inverted at each 90° rotation ($\Lambda_{\mathrm{twist}}/4 = 655$ μm). Vertical dashed lines are the distance corresponding to integer multiples of $\Lambda_{\mathrm{twist}}/4$. As shown in the figure, the S_3 component is constructively accumulated at each $\Lambda_{\mathrm{twist}}/4$, and the generation of a perfect CP mode is possible. The right panel
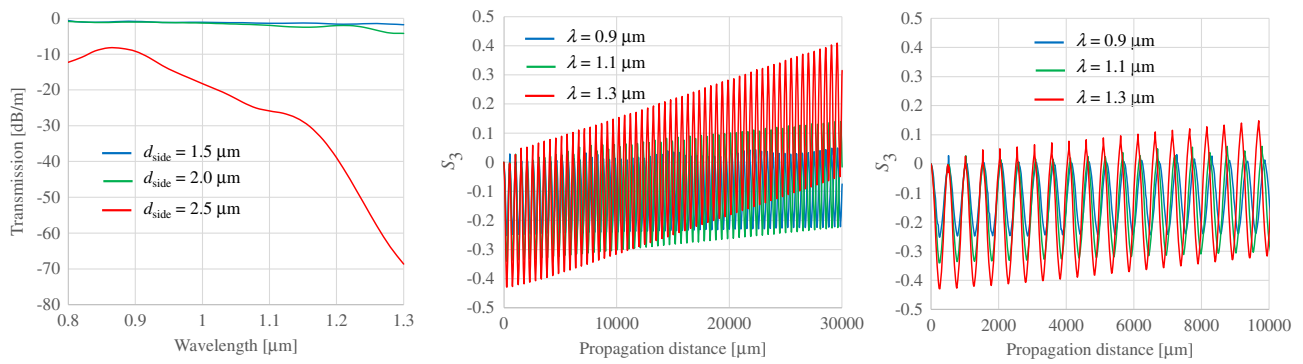

Fig. 8. (Left) Optical power in the core of TB-PCFs and (right) S_3 as a function of propagation distance for different values of α. $d_{\mathrm{side}} = 2.5$ μm.

Fig. 9. (Left) Transmission spectra of TB-PCFs for $\alpha = 0.006$ rad/µm and different values of d_{side}. E_x mode is launched, and the fiber length is 30,000 µm. (Center) S_3 as a function of propagation distance for different wavelength and (right) enlarged view of the center panel.
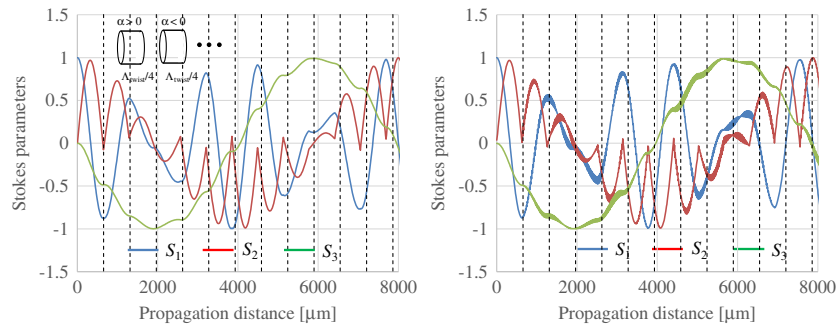

Fig. 10. Stokes parameters of periodically inverted TB-PCF calculated by (left) the analytical method and (right) BPM. $d_{side} = 2.0$ µm and $\alpha = 0.0024$ rad/µm. Dashed vertical lines show the distance of integer multiples of $\Lambda_{twist}/4$.

of Fig. 10 shows the same data, but calculated with BPM. Both results agree very well, and the correctness of the analytical results is confirmed by numerical full-vector simulation.

The left panel of Fig. 11 shows the Poincaré sphere plot of the polarization state of constantly twisted TB-PCF with $d_{side} = 2.0$ µm and $\alpha = 0.0024$ rad/µm. The E_x mode is launched ($S_1 = 1$), and the length of the fiber is 2000 µm. In this case, S_3 is periodically excited as in Fig. 4, and the trajectory on the Poincaré sphere is elliptical. The center panel of Fig. 11 shows the same plot, but with periodic α inversion. At the inversion point, the polarization state trajectory is not continuous, and at 2000 µm, an almost perfect LCP mode is reached (please see Fig. 10). The right panel of Fig. 11 shows the trajectory of the polarization state for $\alpha = 0.006$ rad/µm ($\Lambda_{twist}/4 = 261$ µm). Since the length of one segment is short, the trajectory is more complex. At 2000 µm, an almost perfect LCP mode is obtained, as in the case of $\alpha = 0.0024$ rad/µm. From these results, periodic inversion of the twisting adds a novel degree of freedom to control and generate the arbitrary polarization state.

In the above examples, the value of $\Lambda_{twist}/4$ is some hundreds of micrometers, which is difficult to control if the fiber is cut and spliced. To show the accumulation of the geometric phase for long Λ_{twist}, Fig. 12 shows Stokes parameters

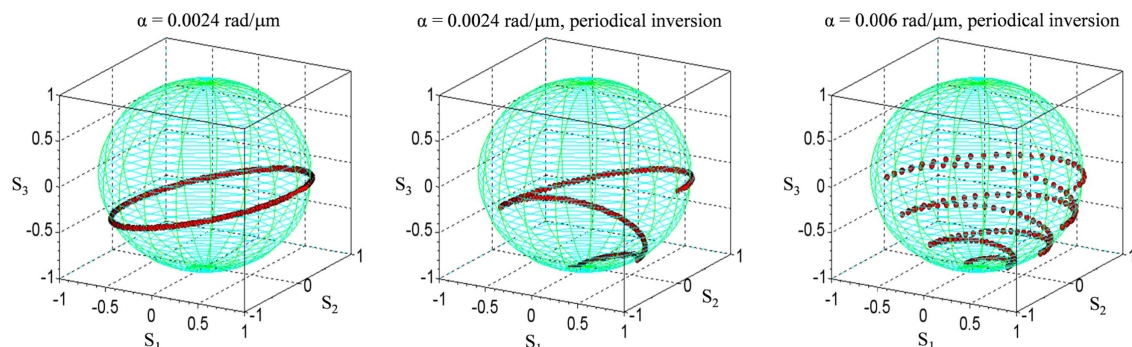**Fig. 11.** Poincaré sphere plots of the polarization state in TB-PCF with $d_{side} = 2.0$ µm. (Left) $\alpha = 0.0024$ rad/µm with constant twisting, (center) $\alpha = 0.0024$ rad/µm with periodically inverted twisting, and (right) $\alpha = 0.006$ rad/µm with periodically inverted twisting.
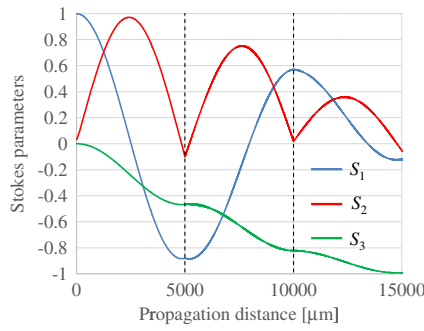
Fig. 12. Stokes parameters of periodically inverted TB-PCF calculated by BPM. $d_{side} = 1.25$ μm and $\alpha = 0.000314$ rad/μm. Dashed vertical lines show the distance of integer multiples of $\Lambda_{twist}/4$.

calculated by BPM for periodically inverted TB-PCF with $d_{side} = 1.25$ μm and $\alpha = 0.000314$ rad/μm ($\Lambda_{twist} = 20{,}000$ μm). The S_3 component is constructively accumulated at each $\Lambda_{twist}/4$, as in the case of Fig. 10.

4. OAM STATE GENERATION IN MULTIMODE TB-PCF

From the results shown in Section 3.E, it is possible to generate an arbitrary polarization state in single-mode TB-PCFs by using periodic twisting inversion. The results lead to a natural extension to a multimode case. For higher-order LP mode, complex polarization evolution in TB-PCF may lead to generating an OAM state with the topological charge ≥1. Here, the generation of the OAM state is shown by launching the usual LP mode to multimode TB-PCF.

The left panel of Fig. 13 shows the cross section of multimode TB-PCF. Seven air holes at the center of the fiber are missing to form a multimode core, and the diameters of two holes are changed to d_{side}. Here, we consider multimode
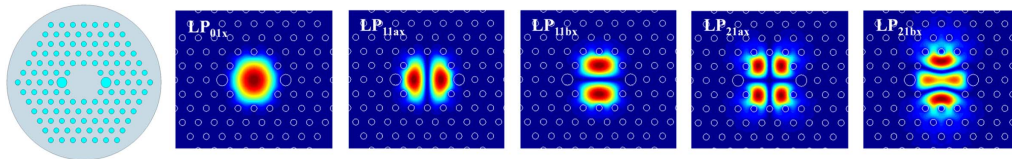
TB-PCF with $d = 1.1$ μm, $\Lambda = 2.9$ μm, and $d_{side} = 2.0$ μm. The twisting rate $\alpha = 0.00314$ rad/μm. The right panels of Fig. 13 show the intensity distributions of the E_x modes (LP_{01}, LP_{11a}, LP_{11b}, LP_{21a}, and LP_{21b}) of the untwisted PCF. There are also E_y modes with intensity patterns similar to E_x modes.

A. Constant Twisting

Here, the polarization evolution in a uniform multimode TB-PCF is investigated. The blue solid line in the left panel of Fig. 14 shows the overlap between input and BPM-propagated fields as a function of propagation distance for LP_{11bx} input. Here, the overlap power is defined as

$$P_{overlap} = \iint E_i \times H_{in}^* dxdy, \tag{14}$$

where E_i is the electric field calculated by BPM at the ith step. H_{in} is the magnetic field of input light. The value of overlap oscillates with an approximately 1000 μm period. Since the 180° rotation period is 1000 μm, the overlap is at a minimum at 90° rotation (500 μm) and increases again at 180° rotation. The periodic nature of the overlap is collapsed for increased propagation distance. This is due to the phase retardation originating from the geometric phase in the twisted PCF. The black dashed line in Fig. 14 shows the total power in the cross section calculated from the Poynting vector. The loss is small in the shown length scale.

At some propagation distances, FFIPs from TB-PCF mixed with the LP_{01x} mode are shown. The FFIP is calculated by [30]

$$\phi_{FFP}(x,y,z) \approx \frac{jk_0 n}{2\pi z} \exp(-jk_0 nz) \iint \phi_{NFP}(x_0,y_0,0)\left(1 - \frac{R^2}{2z^2}\right)$$
$$\times \exp\left(-jk_0 \frac{R}{2z}\right) dx_0 dy_0, \tag{15}$$

where n is the effective index of the free space (in this case 1), ϕ_{NFP} is the near-field pattern (NFP), and $R = \sqrt{(x - x_0)^2 + (y - y_0)^2}$. The FFIP of the output light of

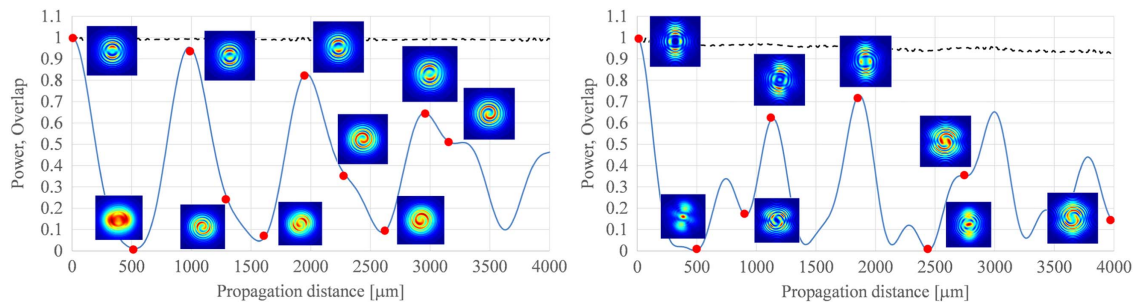**Fig. 13.** Schematic of a multimode TB-PCF and its NFPs.

Fig. 14. Overlap powers (blue solid lines) and total Poynting vectors (black dashed lines) as functions of propagation distance for (left) LP_{11bx} and (right) LP_{21bx} mode input. The inset shows mixed FFIP at the distance marked by red circles.

TB-PCF with 1000 μm free-space propagation and the FFIP of input LP mode with 2000 μm free-space propagation are added. This is the mimic of the typical experiment for OAM observation. The FFIP evolution is very complex, and at some distances, a clear single vortex associated with the OAM state with the topological charge of 1 can be seen. There are both left- and right-handed vortices. This is probably because the propagation constants of all four LP_{11} modes are different, and the relative phase differences between these modes are accumulated and not constant. Therefore, at some point the vortex is left-handed, and at a different point, it is right-handed. It should be noted that to confirm the value of the OAM, numerical evaluation of the mode field is effective [31]. However, in this paper, the "propagated field" containing the components of multiple guided and radiated modes is evaluated and is not the true mode field. Therefore, the numerical evaluation of the OAM for the BPM field is not easy to use to determine the OAM order.

The blue solid line in the right panel of Fig. 14 shows the overlap between input and BPM-propagated fields as a function of propagation distance for LP_{21bx} input. FFIPs at some distances are also shown. The evolution is more complex than that of LP_{11bx} input, and at some distances, a double vortex associated with the OAM state with the topological charge of 2 can be seen. The black dashed line in the right panel of Fig. 14 shows the total power in the cross section calculated from the Poynting vector. The loss is larger compared with the LP_{11} mode input.

B. Periodic Inversion of Twisting

Here, the polarization evolution in TB-PCF with periodic twisting inversion is investigated. The green solid line in the top panel of Fig. 15 shows the overlap between input and BPM-propagated fields as a function of propagation distance for LP_{11bx} input of periodically inverted TB-PCF, together with NFP and FFIP at 1000 and 2350 μm. The period of twisting inversion is 500 μm (90° rotation). The behavior of the overlap value is very complex compared with the constant twisting case (blue dashed line). At 1000 and 2350 μm, doughnut-shaped NFPs are obtained, and left- and right-handed vortex FFIPs are seen. In terms of the value of overlap, it oscillates with an approximately 1000 μm period (π rotation) for a constant twisting fiber. However, the period is slightly shifted from the integer multiples of 500 μm for long-distance propagation, and the value of the overlap becomes small. Since the propagation constants of all four LP_{11} modes are different, the relative phase differences among these modes are accumulated. Therefore, the initial state is not recovered after one rotation, and the difference from the initial state is accumulated during the propagation, resulting in different periods and small overlap. The situation is more complicated in the case of periodic inversion of twisting.

The green solid and blue dashed lines in the bottom panel of Fig. 15 show the same one, but for LP_{21bx} input. The period of twisting inversion is 250 μm (45° rotation). The overlap value seems to have no more periodicity. At 450 and 1800 μm, doughnut-shaped NFPs and double-vortex FFIPs are seen. The black dashed lines in Fig. 15 show the total powers in the cross section calculated from the Poynting vector. As in Fig. 14, the loss is larger for LP_{21} mode input compared with LP_{11} mode input in the shown length range. In addition to these losses, there are intrinsic losses in the real fiber, and they deteriorate the characteristics further.
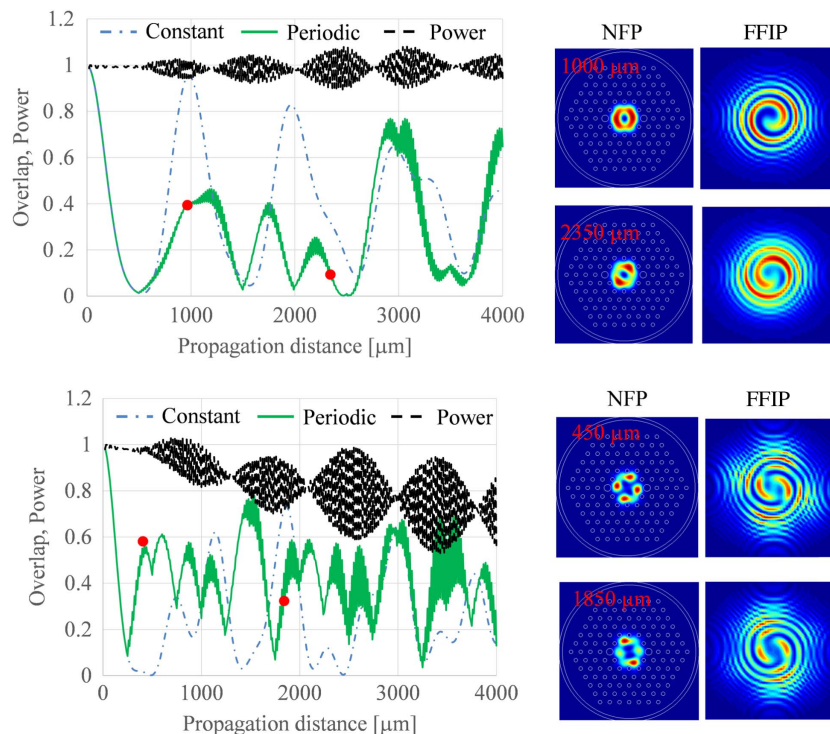

Fig. 15. Overlap powers (green and blue) and total Poynting vectors (black) as functions of periodically inverted multimode TB-PCF for (top) LP_{11bx} and (bottom) LP_{21bx} mode input. The right panels show NFP and mixed FFIP at the distances marked by red circles.

From these results, although OAM states can be generated both in constant and periodically inverted TB-PCFs, a periodically inverted TB-PCF has an additional degree of freedom for controlling the spatial state of light, and there is a possibility that the length can be shortened for generating the OAM state.

5. CONCLUSION

The spatial state of the light (polarization and OAM) in TB-PCFs is theoretically analyzed in terms of the effect of linear birefringence and twisting rate. Recently developed rigorous BPM analysis revealed that the polarization state of light in the TB-PCF is very complex, and some features can be extracted from the analysis. In the TB-PCF with small linear birefringence, the optical activity and the periodic S_3 excitation can be seen. These two features can be explained with the concept of geometric phase existing in the twisted waveguides. Furthermore, a periodically inverted TB-PCF is proposed to control the polarization. By accumulating the phase rotation originating from the geometric phase, an arbitrary polarization state can be generated. In the multimode TB-PCF, the technique may be useful to effectively generate an OAM state. These results indicate that the TB-PCF adds a new degree of freedom to control the spatial state of light and is useful for fiber-based light-controlling devices.

APPENDIX A

Here, the formulation of an analytical beam propagation model in birefringent twisted waveguides used in this paper is summarized. We consider a twisted birefringent waveguide, shown in Fig. 16. The waveguide is twisted along the z direction, and an azimuthal rotation angle is $\theta = \alpha z$. We assume that the reference indices for x- and y-polarized modes are n_x and n_y when $\theta = 0$. In this case, the propagation equation under weak guiding approximation ($\Psi_z \simeq 0$) between z and $z + \Delta z$ is

$$\Psi_{xy}(z + \Delta z) = \begin{bmatrix} \Psi_x(z + \Delta z) \\ \Psi_y(z + \Delta z) \end{bmatrix} = U_{xy} \begin{bmatrix} \Psi_x(z) \\ \Psi_y(z) \end{bmatrix}$$

$$= U_{xy}\Psi_{xy}(z), \tag{A1}$$

$$U_{xy} = \begin{bmatrix} e^{-jk_0 n_x \Delta z} & 0 \\ 0 & e^{-jk_0 n_y \Delta z} \end{bmatrix}, \tag{A2}$$

where Ψ_x and Ψ_y are complex fields of x and y components, and U_{xy} is a propagation matrix. When the waveguide is
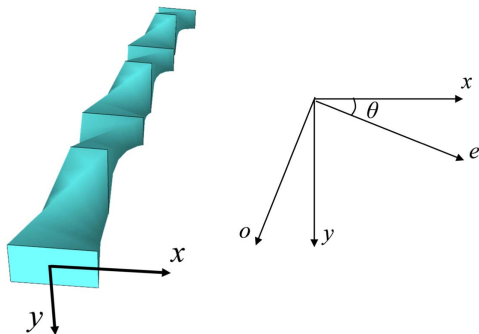

Fig. 16. Schematic of a twisted waveguide and rotated frame.

rotated in the xy plane with the angle θ, we assume the new x and y axes are o and e, as shown in Fig. 16. The complex fields for new axis Ψ_{eo} are given by

$$\Psi_{eo} = \begin{bmatrix} \Psi_e \\ \Psi_o \end{bmatrix} = R(\theta)\Psi_{xy}, \tag{A3}$$

$$R(\theta) = \begin{bmatrix} \cos\theta & \sin\theta \\ -\sin\theta & \cos\theta \end{bmatrix}. \tag{A4}$$

Then, the field propagation in the eo frame is given by

$$\Psi_{eo}(z + \Delta z) = U_{eo}(\theta)\Psi_{eo}(z), \tag{A5}$$

$$\begin{aligned} U_{eo}(\theta) &= R(\theta)U_{xy}R^{-1}(\theta) \\ &= e^{-jk_0 n_{\text{ave}}\Delta z} \begin{bmatrix} \cos\gamma + j\sin\gamma\cos 2\theta & -j\sin\gamma\sin 2\theta \\ -j\sin\gamma\sin 2\theta & \cos\gamma - j\sin\gamma\cos 2\theta \end{bmatrix}, \end{aligned} \tag{A6}$$

where $n_{\text{ave}} = (n_x + n_y)/2$, $\Delta n = n_y - n_x$, and $\gamma = k_0\Delta n\Delta z/2$.

Now, we consider the basis transformation from oe to CP basis. The transformation is given by

$$\Psi_{RL} = \begin{bmatrix} \Psi_R \\ \Psi_L \end{bmatrix} = \frac{1}{\sqrt{2}} \begin{bmatrix} 1 & j \\ 1 & -j \end{bmatrix} \begin{bmatrix} \Psi_o \\ \Psi_e \end{bmatrix} = P^{-1} \begin{bmatrix} \Psi_e \\ \Psi_o \end{bmatrix}, \tag{A7}$$

$$P = \frac{1}{\sqrt{2}} \begin{bmatrix} 1 & 1 \\ -j & j \end{bmatrix}, \tag{A8}$$

where Ψ_R and Ψ_L are complex fields of RCP and LCP components. Therefore, Eq. (A5) is transformed into

$$\Psi_{RL}(z + \Delta z) = U_{RL}(\theta)\Psi_{RL}(z), \tag{A9}$$

$$U_{RL} = P^{-1}U_{eo}P = e^{-jk_0 n_{\text{ave}}\Delta z} \begin{bmatrix} \cos\gamma & j\sin\gamma e^{-2j\theta} \\ j\sin\gamma e^{2j\theta} & \cos\gamma \end{bmatrix}. \tag{A10}$$

Here, an additional phase given by $e^{2j\theta}$ with an opposite sign in nondiagonal terms is called a geometric phase. By using these equations, the evolution of input light (CP or LP mode) in the rotated frame can be calculated easily. If Δz is sufficiently small, the beam propagation in the twisted waveguides can be treated by concatenating two segments: θ and $\theta + \Delta\theta$.

Disclosures. The authors declare no conflicts of interest.

REFERENCES

1. V. I. Kopp, V. M. Churikov, J. Singer, N. Chao, D. Neugroschl, and A. Z. Genack, "Chiral fiber gratings," Science **305**, 74–75 (2004).
2. V. I. Kopp, V. M. Churikov, G. Zhang, J. Singer, C. W. Draper, N. Chao, D. Neugroschl, and A. Z. Genack, "Single- and double-helix chiral fiber sensors," J. Opt. Soc. Am. B **24**, A48–A52 (2007).
3. G. Shvets, S. Trendafilov, V. I. Kopp, D. Neugroschl, and A. Z. Genack, "Polarization properties of chiral fiber gratings," J. Opt. A **11**, 074007 (2009).

4. M. Napiorkowski and W. Urbanczyk, "Rigorous simulations of coupling between core and cladding modes in a double-helix fiber," Opt. Lett. **40**, 3324–3327 (2015).

5. G. K. L. Wong, M. S. Kang, H. W. Lee, F. Biancalana, C. Conti, T. Weiss, and P. St. J. Russell, "Excitation of orbital angular momentum resonances in helically twisted photonic crystal fiber," Science **337**, 446–449 (2012).

6. X. M. Xi, T. Weiss, G. K. L. Wong, F. Biancalana, S. M. Barnett, M. J. Padgett, and P. St. J. Russell, "Optical activity in twisted solid-core photonic crystal fibers," Phys. Rev. Lett. **110**, 143903 (2013).

7. T. Weiss, G. K. L. Wong, F. Biancalana, S. M. Barnett, X. M. Xi, and P. St. J. Russell, "Topological Zeeman effect and circular birefringence in twisted photonic crystal fibers," J. Opt. Soc. Am. B **30**, 2921–2927 (2013).

8. G. K. L. Wong, X. M. Xi, M. H. Frosz, and P. St. J. Russell, "Enhanced optical activity and circular dichroism in twisted photonic crystal fibers," Opt. Lett. **40**, 4639–4642 (2015).

9. C. Fu, S. Liu, Y. Wang, Z. Bai, J. He, C. Liao, Y. Zhang, F. Zhang, B. Yu, S. Gao, Z. Li, and Y. Wang, "High-order orbital angular momentum mode generator based on twisted photonic crystal fiber," Opt. Lett. **43**, 1786–1789 (2018).

10. T. Fujisawa and K. Saitoh, "Off-axis core transmission characteristics of helically twisted photonic crystal fibers," Opt. Lett. **43**, 4935–4938 (2018).

11. L. Zang, M. S. Kang, M. Kolesik, and P. St. J. Russell, "Dispersion of photonic Bloch modes in periodically twisted birefringent media," J. Opt. Soc. Am. B **27**, 1742–1750 (2010).

12. S. Rashleigh, "Origins and control of polarization effects in single-mode fibers," J. Lightwave Technol. **1**, 312–331 (1983).

13. S. Slussarenko, A. Alberucci, C. P. Jisha, B. Piccirillo, E. Santamato, G. Assanto, and L. Marrucci, "Guiding light via geometric phase," Nat. Photonics **10**, 571–575 (2016).

14. T. Fujisawa, T. Sato, and K. Saitoh, "Full-vector finite-element beam propagation method for helicoidal waveguides and its application to twisted photonic crystal fiber," J. Lightwave Technol. **35**, 2894–2901 (2017).

15. T. Fujisawa, T. Sato, and K. Saitoh, "Errata to 'Full-vector finite-element beam propagation method for helicoidal waveguides and its application to twisted photonic crystal fiber'," J. Lightwave Technol. **36**, 4211–4212 (2018).

16. S. Nakano, T. Fujisawa, T. Sato, and K. Saitoh, "Beam propagation analysis of optical activity and circular dichroism in helically twisted photonic crystal fiber," Jpn. J. Appl. Phys. **57**, 08PF06 (2018).

17. Y. Yan, J. Wang, L. Zhang, J.-Y. Yang, I. M. Fazal, N. Ahmed, B. Shamee, A. E. Willner, K. Birnbaum, and S. Dolinar, "Fiber coupler for generating orbital angular momentum modes," Opt. Lett. **36**, 4269–4271 (2011).

18. H. Xu and L. Yang, "Conversion of orbital angular momentum of light in chiral fiber gratings," Opt. Lett. **38**, 1978–1980 (2013).

19. L. Fang and J. Wang, "Flexible generation/conversion/exchange of fiber-guided orbital angular momentum modes using helical gratings," Opt. Lett. **40**, 4010–4013 (2015).

20. H. Wu, S. Gao, B. Huang, Y. Feng, X. Huang, W. Liu, and Z. Li, "All-fiber second order vortex generation based on strong modulated long-period grating in a four-mode fiber," Opt. Lett. **42**, 5210–5213 (2015).

21. A. Nicolet, F. Zolla, Y. O. Agha, and S. Guenneau, "Geometrical transformations and equivalent materials in computational electromagnetism," COMPEL **27**, 806–819 (2011).

22. A. Nicolet and F. Zolla, "Finite element analysis of helicoidal waveguides," IET Sci. Meas. Technol. **1**, 67–70 (2007).

23. A. Nicolet, F. Zolla, Y. O. Agha, and S. Guenneau, "Leaky modes in twisted microstructured optical fibers," Waves Random Complex Media **17**, 559–570 (2007).

24. J. B. Pendry, D. Schurig, and D. R. Smith, "Controlling electromagnetic fields," Science **312**, 1780–1782 (2006).

25. K. Okamoto, *Fundamentals of Optical Waveguides* (Academic, 2006).

26. T. Fujisawa and M. Koshiba, "Finite element characterization of chromatic dispersion in nonlinear holey fibers," Opt. Express **11**, 1481–1489 (2003).

27. E. Hecht, *Optics*, 2nd ed. (Addison-Wesley, 1987).

28. M. Napiorkowski and W. Urbanczyk, "Role of symmetry in mode coupling in twisted microstructured optical fibers," Opt. Lett. **43**, 395–398 (2018).

29. M. Napiorkowski and W. Urbanczyk, "Scaling effects in resonant coupling phenomena between fundamental and cladding modes in twisted microstructured optical fibers," Opt. Express **26**, 12131–12143 (2018).

30. S. Nakano, T. Fujisawa, and K. Saitoh, "The effect of core offset on the mode converting characteristics in twisted single mode fibers," J. Lightwave Technol. **37**, 5479–5485 (2019).

31. M. F. Picardi, K. Y. Bliokh, F. J. Rodriguez-Fortuno, F. Alpeggiani, and F. Nori, "Angular momenta, helicity, and other properties of dielectric-fiber and metallic-wire modes," Optica **5**, 1016–1026 (2018).